

Chapter 10. Underwater Topography

Werner Alpers

Institut für Meereskunde, Universität Hamburg, Hamburg Germany

Gordon Campbell

European Space Agency, ESRIN, Frascati, Italy

Han Wensink

ARGOSS, Vollenhove, The Netherlands

Quanan Zhang

Graduate College of Marine Studies, University of Delaware, Newark, DE, USA

10.1 Introduction

Knowledge of underwater features and ocean bathymetry is essential to support activities such as shipping, boating, dredging, pipeline and cable laying, and for the determination of coastal hazards. In certain areas (for example the Dutch and the German coasts) the location, shape, and depth of underwater banks or shoals is highly variable due to the presence of strong currents and a seafloor that consists of sand or gravel. Under these conditions, regular monitoring and dredging are required in coastal areas. Conventionally, depth charts are obtained by sonar measurements carried out from dedicated vessels (survey vessels), which are quite expensive to operate with typical operating costs of US \$5000 per day.

Under favorable conditions, synthetic aperture radar (SAR) has the ability to detect sea floor topographic features in shallow water areas. The radar detects underwater features indirectly by means of variations of the sea surface roughness induced by variations of a current overflowing the submarine feature. Thus this technique relies on the presence of a (strong) current, along with the presence of small-scale waves (wind waves) on the sea surface to provide the radar backscatter. While at present it is not possible to generate depth charts from radar data alone (acoustic sounding data must be used for calibration), the data can be used to highlight areas of significant change, or to interpolate between depth profiles measured by acoustic sounders operated from ships. Thus radar measurements can serve to reduce greatly the number of ship tracks required for generating bathymetric maps of a given accuracy and therefore can reduce greatly the costs of bathymetric surveying.

In Section 10.2 the principle of radar imaging of underwater topography is described and in Section 10.4 a more detailed description of the present status of the synthetic aperture radar (SAR) imaging theory is given. Some representative examples of SAR images showing bathymetric features acquired by satellite SARs are presented in Section 10.3. A method that uses (in conjunction with acoustic sounding data) ERS SAR data to generate bathymetric maps is described in Section 10.5. An assessment of the accuracy of this method, called Bathymetry Assessment System (BAS) and developed by ARGOSS in the Netherlands, is also presented in Section 10.5. Finally, Section 10.6 contains a short summary and a historical note.

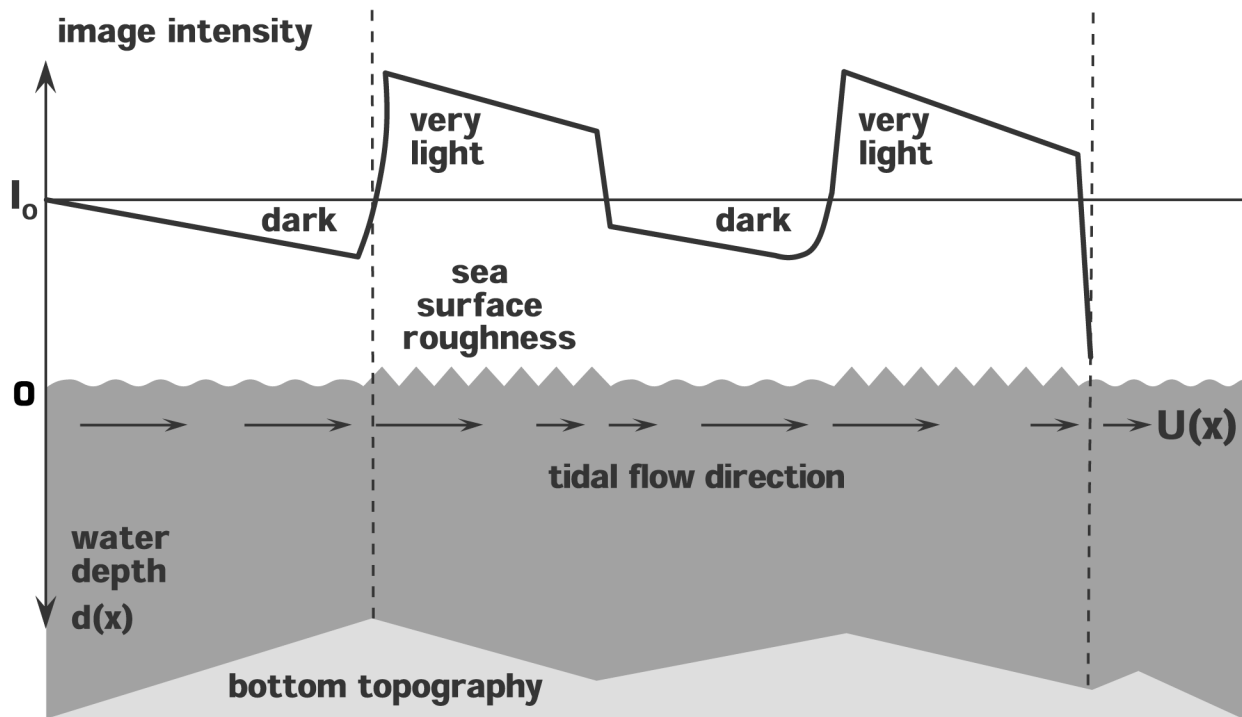


Figure 10.1. Schematic plot showing the relationship between radar image intensity, sea surface roughness, tidal flow, and underwater bottom topography.

10.2 Principle of radar imaging of underwater bottom topography

It has been known for more than thirty years that, under certain conditions, underwater topographic features, like (sand) banks and shoals, become visible on radar images of the sea surface. This is surprising because the electromagnetic waves emitted by the radar penetrate into sea water only to a depth that is small compared to the radar wavelength, i.e., to a depth on the order of millimeters to centimeters depending on radar wavelength. Already in 1969, *de Loor* and coworkers in the Netherlands noticed radar signatures of underwater sand waves on Ka-band (36 GHz) real aperture radar (RAR) images taken from an aircraft over the North Sea [*de Loor and Brunsveld van Hulsten, 1978*]. However, the knowledge that radar is capable of detecting underwater bottom features down to depths of tens of meters below the sea surface in ocean regions with strong (usually tidal) currents became widespread only in 1978 when the first radar images acquired by the synthetic aperture radar (SAR) aboard the American SEASAT satellite became available. In particular, SEASAT SAR images acquired over the English Channel and the Nantucket Shoals have been used extensively in studies dealing with the radar imaging mechanism of underwater sand banks [*Lodge, 1983; Alpers and Hennings, 1984; Shuchman et al., 1985; Valenzuela et al., 1985; Hennings et al., 1988*].

Imaging radars like real aperture radar (RAR) or synthetic aperture radar (SAR) sense underwater topographic features indirectly by variations of the small-scale sea surface roughness induced by a variable surface current. The radar imaging mechanism of an underwater topographic feature (sand wave) is depicted schematically in Figure 10.1 [*Alpers and Hennings, 1984; Shuchman et al., 1985; Vogelzang et al., 1992; Vogelzang, 1997*]. The tidal current is modified by the variable water depth as indicated by the arrows. The current velocity at the sea surface is higher over shallow areas than over deep areas, giving rise to convergent flow regimes where the sea surface roughness is increased and to divergent flow regimes where roughness is

Underwater Topography

decreased. In the convergent areas, the waves are "squeezed", while in the divergent areas they are "stretched". This leads in the convergent areas to an increase of the amplitude of the Bragg waves responsible for the radar backscattering (see Section 10.4) and thus to an increase of the backscattered radar power; in the divergent areas it leads to a decrease in Bragg wave amplitude. Therefore on radar images the convergent areas appear as areas of enhanced image intensity and the divergent areas as areas of reduced image intensity. In most cases, the surface current is a tidal current. The strongest modulation of the sea surface roughness and thus the strongest variation of the backscattered radar signal is obtained when the tidal velocity is at its peak value. At slack tide, when the tidal velocity is zero, no topographic features can be delineated on radar images.

As mentioned in the introduction, a second prerequisite for underwater topographic features to become visible on radar images is the presence of Bragg waves on the sea surface. The wind-generated waves provide the small-scale surface roughness needed for the backscattering of the microwaves [Valenzuela, 1978]. Thus, the wind speed must be above the threshold for small-scale wave generation, (i.e., the wind speed has to be above 2 to 3 m s^{-1}). But the wind speed has also to be below 8 to 10 m s^{-1} where the wind induced roughness would mask the modulation of the small-scale water waves by the underwater topography. The optimum wind speed for detecting underwater bottom topography is 3 to 6 m s^{-1} .

Thus in order to retrieve depth information from radar images of the sea surface, one has to have a good knowledge of the three processes contributing to the radar imaging mechanism: (1) the interaction of the current with the underwater topographic features, (2) the modulation of the sea surface roughness by the surface current (hydrodynamic modulation), and (3) the interaction of the electromagnetic (radar) wave with the sea surface. Today there exists good models to describe all three processes; but some uncertainties remain. In particular, the second process constitutes the weakest link in the procedure to invert radar images into quantitative depth charts. The modulation of the short water waves depends strongly on wind speed and wind direction relative to the current direction [Romeiser and Alpers, 1997]. Therefore, present inversion schemes rely on some kind of tuning by data obtained from conventional acoustic depth sounding. A more detailed description of these processes is presented in Section 10.4.

10.3 Examples of SAR images showing underwater topographic features

In this section we present some examples of SAR images showing underwater topographic (or bathymetric) features acquired by the L-band SAR aboard the American SEASAT satellite, the C-band SAR aboard the European ERS-1 and ERS-2 satellites, and the C-band SAR aboard the European ENVISAT satellite launched on 1 March 2002. Imagery from these satellites shows that underwater topography is visible in a number of coastal regions around the world. Examples of such areas include the German, Dutch, Belgian, and French coasts, the Taiwan Tan Shoals located between Taiwan and Mainland China, the Strait of Malacca separating the Malay Peninsula from the Indonesian island of Sumatra; the Xinchuan Gang Shoals off the east coast of China north of Shanghai, the Nantucket Shoals off the coast of Massachusetts, USA, and the Bay of Bengal near the Mouths of the Ganges.

Figure 10.2 shows a SEASAT SAR image of the northeastern approach to the English Channel. This image was acquired on 19 August 1978 at 0646 UTC (orbit 762). The center of the imaged area is located at $51^{\circ}32'N$, $2^{\circ}05'E$. On the right-hand side of the image, the French-Belgian coast is visible with the French town Calais at the bottom. The V-shaped feature in the lower left-hand section of the image is a pair of two underwater ridges called South Falls (the

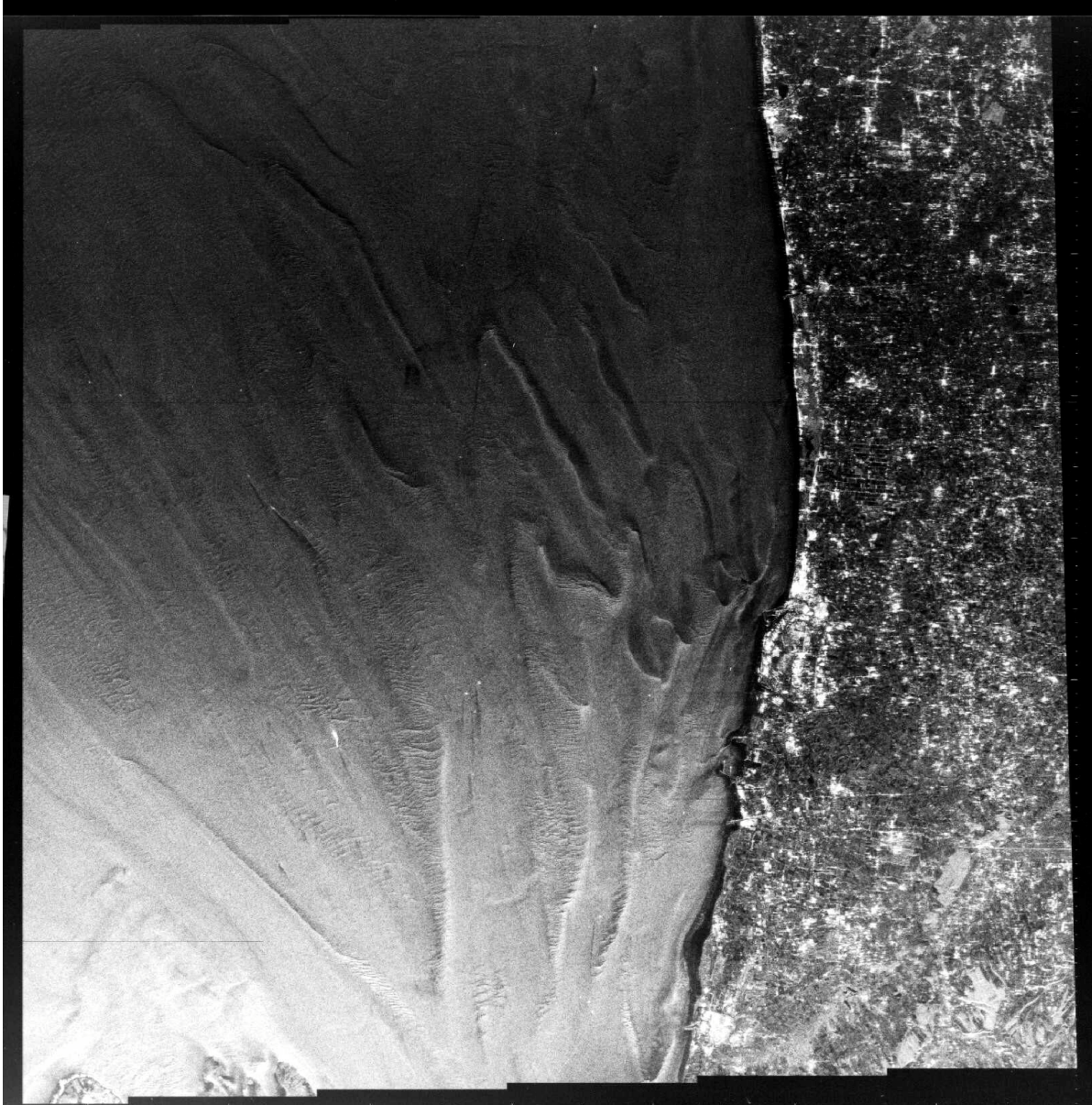


Figure 10.2. SEASAT (L-band, HH) SAR image of the northeastern approach to the English Channel acquired 19 August 1978. Visible on the right-hand side is the French/Belgian coast. (Because this image is not corrected for the variation of brightness with incident angle, the image intensity is high along the left side of the image corresponding to near range [steep incident angles].) The imaged area is 100 km x 100 km.

thin line to the left) and Sandettie (the broader line to the right). South Falls is about 30 km long and 600 to 800 m broad and rises to within 7 m of the sea surface. The seafloor between the two ridges has a depth between 30 and 40 m. At the time of the SAR data acquisition the tidal flow was directed toward the southwest with a speed between 1.7 and 2.4 m s^{-1} . The wind speed was 4 m s^{-1} . Thus optimum SAR imaging conditions were encountered: the tidal current velocity was close to its peak value during the tidal cycle and the wind speed was well above threshold for small-scale wave generation (above 2 to 3 m s^{-1}), but not too high (above 8 m s^{-1}) such that the sea surface roughness modulation caused by the variable current associated with the tidal flow over the sand banks was masked by wind effects.

Underwater Topography

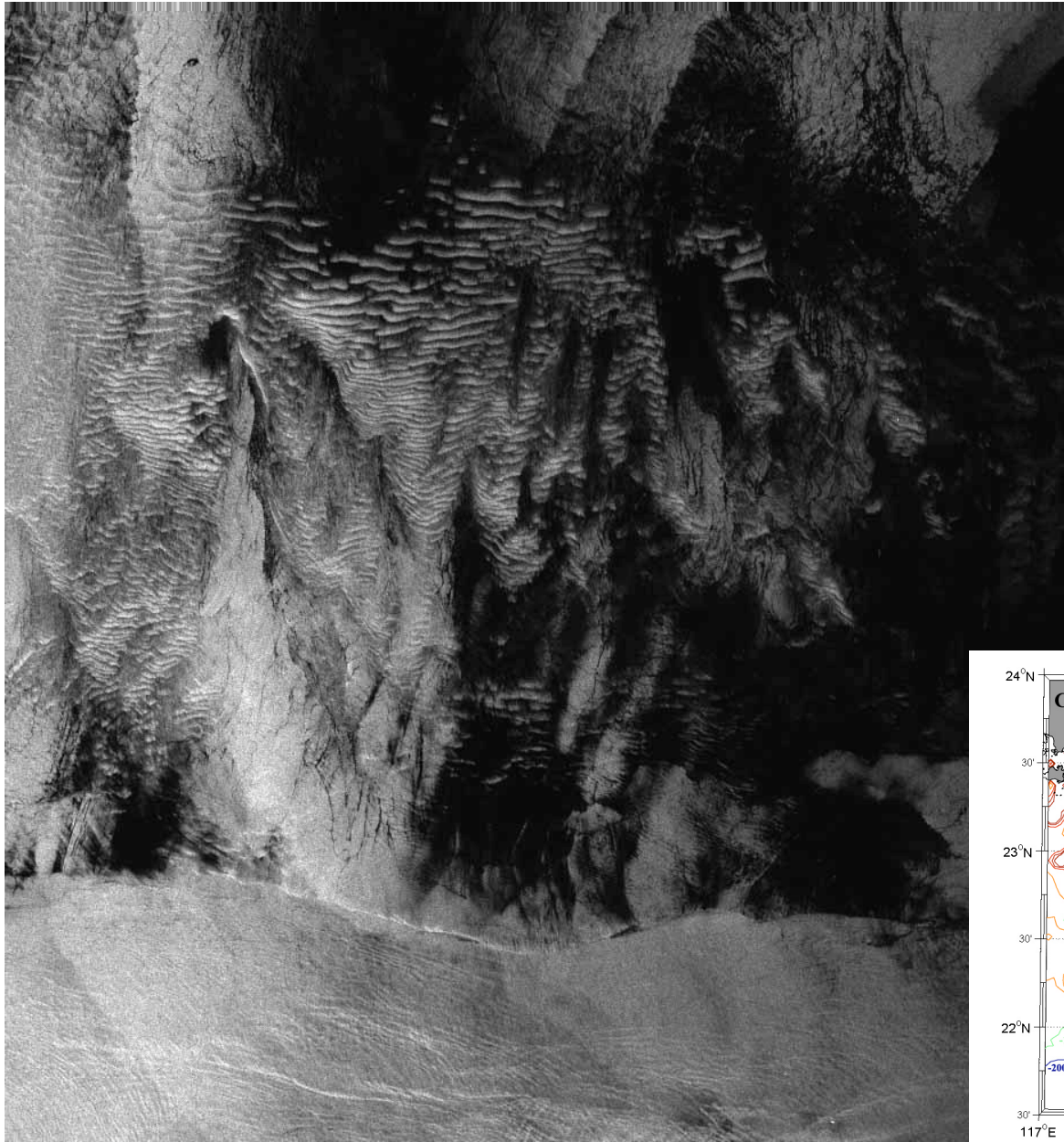
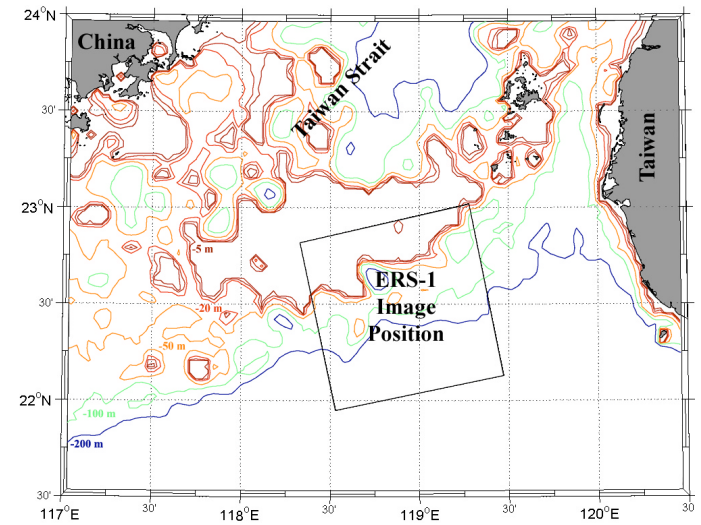


Figure 10.3. (left) ERS-1 (C-band, VV) SAR image of the central part of the Taiwan Tan Shoals (see Figure 10.4) acquired 27 July 1994. The water depth in most of the shallow areas (the areas to the North showing wave-like patterns in the image) is between 10 m and 20 m. The Taiwan current is visible in the lower section of the image. The bright streaks are sea surface manifestations of current fronts that closely follow the depth lines. The imaged area is 100 km x 100 km. ©ESA 1994

Figure 10.4. (below) Location of the imaged area depicted in Figure 10.3. Mainland China is located to the left and Taiwan to the right. Depth contours are in meters (-200 (blue), -100, -50, -20, -10 and -5 (dark red))



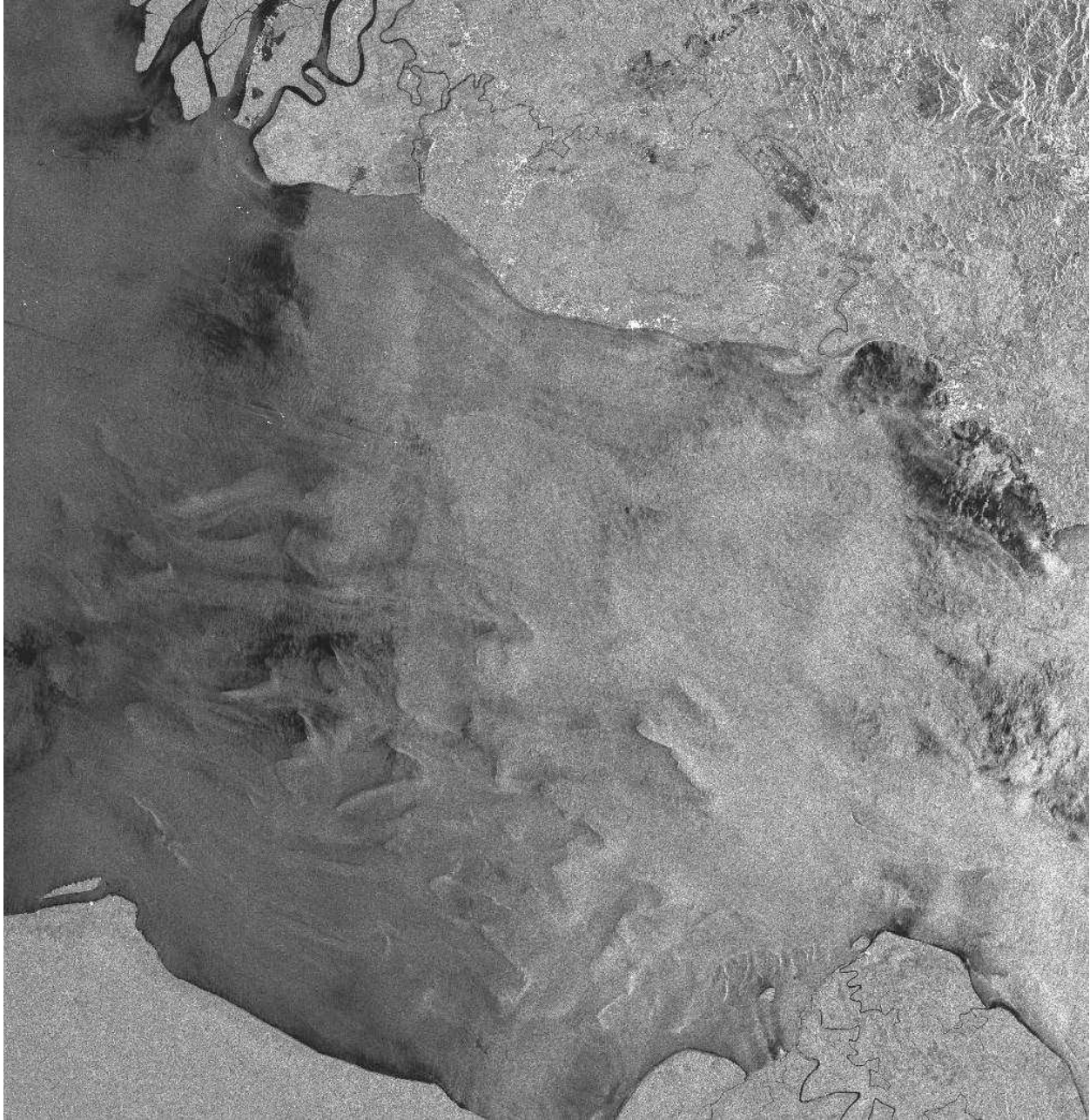


Figure 10.5. ERS-1 (C-band, VV) SAR image acquired 10 May 1996 showing a section of the Strait of Malacca separating the Malayan Peninsula (at the top) from the Indonesian island of Sumatra (at the bottom). The land area in the lower right-hand section of the image is the Indonesian Island Rupert. Northeast of Rupert sea surface manifestations of sandbanks are visible. The sandbanks are quite shallow (typically only a few meters deep). The bright spots visible in the northern section of the strait are ships. The imaged area is 100 km x 100 km. ©ESA 1996

Figure 10.3 shows an ERS-1 SAR image of the central part of the Taiwan Tan Shoals. The location of the imaged area is depicted in Figure 10.4. This image was acquired on 27 July 1994 at 1431 UTC (orbit 158509, frame 459). The Taiwan Tan Shoals are located in the southern part of the Taiwan Strait between 22.5° to 23.3° N and 117.8° to 119.2° E. They are one of the largest shoals in the world's ocean covering an area of about $10,000 \text{ km}^2$. In most parts of the Taiwan Tan Shoals, the water depth is between 10 and 20 m, but there are also some isolated

Underwater Topography



Figure 10.6. ERS-1 (C-band, VV) SAR image acquired 1 July 1999 showing a section of the Strait of Malacca which is located south of the area shown in Figure 10.5, but with overlapping areas. The island in the center of the image is the Indonesian Island Rupert. The sandbanks north/northeast of Rupert are also visible on the ERS-1 SAR image depicted in Figure 10.5. Note that the radar signatures of the same sandbanks are quite different on both ERS SAR images due to different flow and atmospheric conditions. The imaged area is 100 km x 100 km. ©ESA 1999.

areas that fall dry during ebb tide. To the south, the bottom depth first increases slowly and then rapidly. At this slope the northward flowing Taiwan current is deflected to the east. The Taiwan Tan Shoals consist of ridges which are separated by channels and of sand waves. The orientation of the sand waves is approximately perpendicular to the direction of the major axis of the tidal ellipse, i.e., from NNW/NWW to SSE/SEE. The wavelength of the sand waves varies between 300 m and 2000 m and the peak-to-trough amplitude can sometimes exceed 20 m. Most of the

top sediments are composed of medium coarse sands that can be advected by strong currents. The Taiwan current is visible in the lower section of the image. The bright streaks are sea surface manifestations of current fronts that closely follow the depth lines. During the ERS-1 SAR data acquisition a light wind was blowing.

Figure 10.5 shows an ERS-1 SAR image of a section of the Strait of Malacca. The central coordinates of the imaged area are $2^{\circ}32'N$ $101^{\circ}27'E$. This image of dimension 100 km x 100 km was acquired on 10 May 1996 at 335 UTC (orbit 25199, frame 3555). At the bottom of the image the coast of Sumatra is visible and at the top the coast of Malaysia is seen. The land area visible in the lower right-hand section of the image is the Indonesian island Rupa, and the river delta in the upper left-hand section is the river system on which the port of Kuala Lumpur, Kelang, is located. The irregular features in the lower section of the image are sea surface manifestations of sandbanks. At the time of the SAR data acquisition the tidal flow was directed eastwards. The sandbanks in this region are only a few meters deep and some of them even fall dry at low tides. The shipping lane is located north of this area.

Figure 10.6 shows an ERS-2 SAR image of a section of the Strait of Malacca, which partly overlaps with the section shown in Figure 10.5. The central coordinates of the imaged area are $1^{\circ}54'N$, $101^{\circ}14'E$. This image of dimension 100 km x 100 km was acquired on 1 July 1999 at 1553 UTC (orbit 21938, frame 27). Note that on this SAR image the sea surface manifestations of the same sandbanks differ significantly from the ones visible on the previous SAR images. This is due to different flow and atmospheric conditions on both days.

Figure 10.7 shows an ENVISAT ASAR image acquired on 21 August 2002 over the Strait of Dover. Sandbanks can be clearly delineated. The bright area in the lower left-hand section of the image results from enhanced local wind in this area. Fluctuations of the wind speed and direction at the sea surface are less visible on SEASAT SAR images than on ERS and ENVISAT SAR images. This is mainly due to the fact that SEASAT SAR was an L-band SAR operating at a radar frequency of 1.275 GHz corresponding to a wavelength of 23.5 cm, while the ERS and ENVISAT SARs are C-band SARs operating at a frequency of 5.3 GHz corresponding to a wavelength of 5.7 cm. Thus, the wavelength of the Bragg waves (i.e., of those small-scale water waves that are responsible for the radar backscattering) is more than a factor four larger for SEASAT SAR than for ERS or ENVISAT SAR. It is intuitively evident that the longer SEASAT Bragg waves (wavelength approximately 30 cm) respond much slower to wind fluctuations than ERS/ENVISAT SAR Bragg waves [Weissman *et al.*, 1996]. Thus, as a consequence of the longer radar wavelength, underwater bottom features are better visible on SEASAT SAR images than on ERS/ENVISAT SAR images because they are less corrupted by wind effects. Another, but probably minor factor contributing to the better visibility of oceanic phenomena on SEASAT SAR images as compared to ERS SAR images is the difference in polarization. SEASAT SAR operated at horizontal/horizontal (HH) polarization, while ERS SAR operates at vertical/vertical (VV) polarization. However, ENVISAT SAR (ASAR) can operate in HH, VV as well as in cross polarization (VH or HV).

As will be discussed in Section 10.4.3, second-order scattering theory [Romeiser and Alpers, 1997] predicts that the modulation of the backscattered radar power is stronger at HH polarization than at VV polarization. This has also been confirmed experimentally. However, the difference in polarization between SEASAT SAR and ERS SAR very likely contributes little to the difference in the observed modulation depths

Figure 10.8 shows an ERS-1 SAR image of the near-shore section of the Xinchuan Gang (Subei) Shoal off the coast of China. The image was acquired on 8 July 1995 at 0234 UTC

Underwater Topography



Figure 10.7. ENVISAT (C-band, VV) ASAR image of the Strait of Dover (English Channel) acquired on 21 August 2002. The image shows the English coast with the Thames estuary (upper left) along with a section the French and Belgian coasts (lower right). Underwater bottom features can be delineated east of the Thames estuary and north of the Belgian coast. ©ESA 2002

(orbit 20804, frame 2943). The imaged area of dimension 100 km x 100 km is depicted in the map shown in Figure 10.9. Its center is located at $32^{\circ}56'N$, $121^{\circ}12'E$. The light gray area in the left-hand side and at the bottom of the image is land. The irregular dark band adjacent to the coast and the dark areas farther off the coast are tidal flats that have fallen dry. The light-gray patterns in the right-hand section of the image are submerged sand ridges, which are quite similar to the underwater sand ridges visible in Figure 10.2.



Figure 10.8. ERS-1 (C-band, VV) SAR image acquired 8 July 1995 showing the Xinchuan Gang (Subei) Shoal off the coast of China (north of Shanghai). The dark areas are sea areas that have fallen dry during ebb tide. (Also, because this image is not corrected for the variation of the image brightness with incident angle, the image intensity is high in the lower section of the image corresponding to near range [steep incident angles].) The imaged area is 100 km x 100 km. ©ESA 1995

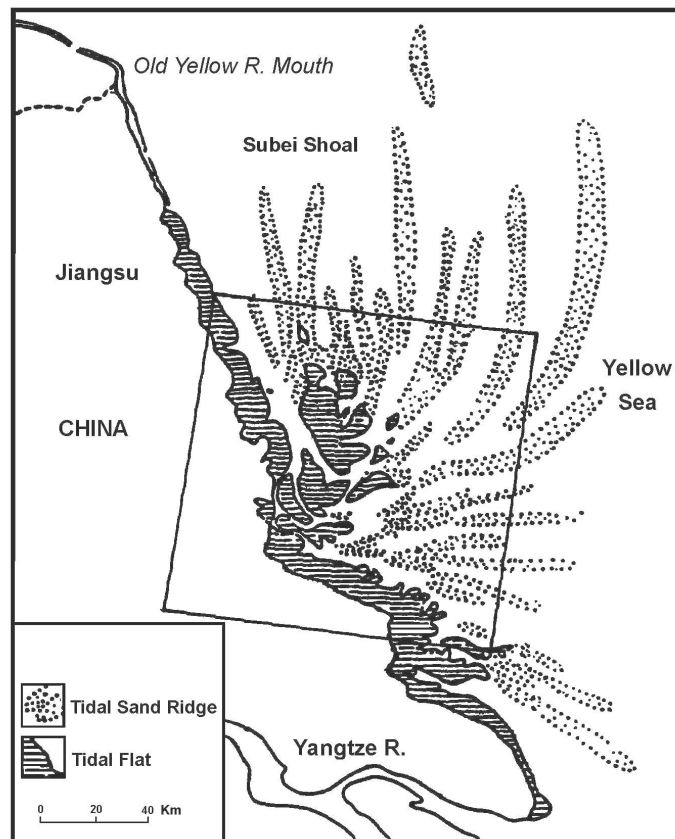


Figure 10.9. Map of the Xinchuan Gang (Subei) Shoal located off the Chinese coast. The inserted box marks the imaged area shown in Figure 10.8.

10.4 Theory of radar imaging of underwater bottom topography

As stated in Section 10.2, three processes are involved in the radar imaging mechanisms of underwater topography: (1) the interaction of the current with the underwater topographic features, (2) the modulation of the sea surface roughness by the surface current (hydrodynamic modulation), and (3) the interaction of the electromagnetic (radar) wave with the sea surface. These three processes are now discussed in more detail.

10.4.1 Current-bottom topography interaction

The interaction of a three-dimensional time variable current with a three-dimensional underwater bottom topographic feature can be a very complex process which requires extensive mathematical modeling [see, e.g., *Loder, 1980, Loder et al., 1992*]. In these numerical models the conservation of mass equation together with the two-dimensional shallow water hydrodynamic equations are solved. Input parameters are: (1) depth averaged flow, (2) surface wind stress, (3) bottom friction, (4) reference height of the water, (5) local elevation of the water relative to the reference height, (6) Coriolis force, (7) water density, and (8) underwater bottom topography. As model output, the perturbation of the surface current imposed by the bottom topography is obtained. For many specific underwater topographic features, simplifications are possible. Often one assumes that the current flow above the topography is laminar, free of vertical current shear, and only weakly time-dependent. If applied to a long underwater ridge or long sand wave, one can approximate the interaction of the flow above with the obstacle as follows: the velocity component normal to the direction of the ridge or sand wave obeys the continuity equation and the velocity component parallel to it remains constant [*Alpers and Hennings, 1984*]

Of course, when aiming at inverting radar images into bathymetric maps, the bottom topography is unknown. But as stated in the introduction, at present it is impossible to retrieve bathymetric maps from radar images by using a stand-alone radar-imaging model that is not calibrated by acoustic data. Usually, the inversion scheme for retrieving bathymetric maps from radar data starts with a first-guess coarse-grid bathymetric map obtained from sounding data. Then the best-fit bathymetric map is determined by an iterative procedure.

10.4.2 Wave-current interaction

All theories developed so far for describing the modulation of the short-scale ocean waves by a variable current induced by a tidal flow over underwater topographic features are based on weak hydrodynamic interaction theory [see, e.g., *Longuet-Higgins and Stewart, 1964*]. The underlying equation is the action balance equation. The theories differ only in the parameterization of the source function that describes the combined effect of wind input, non-linear wave-wave interaction, and dissipation by wave breaking. In combination, these three processes force a wave spectrum that has been perturbed by a variable surface current always back to its equilibrium state. The time it takes a wave to resume its equilibrium amplitude after perturbation is called relaxation time. The larger the relaxation time, the longer the wave can keep its imbalance (non-equilibrium) caused by the variable current, and thus the stronger is the modulation of the wave amplitude by the variable current. Obviously, the relaxation time must be a function of the wavelength of the water wave and of the wind speed. It turns out that the larger the wavelength and the lower the wind speed, the larger is the relaxation time. This has been confirmed in experiments carried out in the laboratory as well as in the field (open ocean).

A theory describing the modulation of the wave spectrum by a variable current using the action balance equation, where the source function is approximated by a linear term in the spectral energy density of the water waves, was first presented by *Alpers and Hennings* [1984]. If this model is reduced to the one-dimensional case and if it is assumed that the advection time (i.e., the characteristic time during which the current varies) is large compared to the relaxation time, then this model yields the result that the relative variation of the spectral energy density, or of the square of the wave amplitude, is equal to the gradient of the surface current multiplied by the relaxation time. It turns out that already this first-order hydrodynamic interaction model can explain qualitatively many basic features observed in radar images showing underwater bottom topographic features.

However, despite the ability of the first-order hydrodynamic interaction theory to describe qualitatively or semi-quantitatively many observed phenomena, it has obvious shortcomings.

A hydrodynamic model capable of describing quantitatively the wave-current interaction at all wavelengths and wind speeds is presently not available. There have been many attempts to improve the first-order theory by including a second order term in the source function [*Shuchman et al.*, 1985, *Thompson and Gasparovic*, 1986; *Trulsen et al.*, 1990] or even higher order terms [*Donelan and Pierson*, 1987]. Still, the current-wave interaction module remains the weakest link in the inversion of radar images into bathymetric maps when trying to abstain from any soundings for calibration.

10.4.3 Radar-ocean wave interaction

The dominant radar backscattering mechanism responsible for radar backscattering from the rough ocean surface at incident angles, θ , between 20 and 70 degrees is Bragg scattering [*Valenzuela*, 1978]. According to Bragg scattering theory, the backscattered radar power or the normalized radar cross section (NRCS) is proportional to the spectral energy density of those waves which travel away or towards the radar look direction and which have wavelengths λ_B which are related to the radar wavelength, λ , and the incident angle, θ , by the Bragg resonance condition:

$$\lambda_B = \lambda / 2 \sin \theta.$$

This simple Bragg scattering model was used in the early imaging models developed by *Alpers and Hennings* [1984] and *Shuchman et al.* [1985] for describing the radar imaging of underwater bottom topography. In these models, the relative variation of the normalized radar cross section is equal to the relative variation of the spectral energy density of the Bragg waves, which implies that the modulation is independent of polarization. This means that, if this model were correct, there would be no difference in the modulation depth between radar images acquired at vertical and horizontal polarization. Another prediction of this first order model is that underwater bottom features are better visible on L-band radar images than on C-band radar images, because at L-band the water waves responsible for the radar backscattering (the Bragg waves) have a longer wavelength than at C-band (approximately four times longer). As discussed in Section 10.4.2, the longer the Bragg wavelength, the longer the relaxation time. This results in a larger modulation of the spectral energy density of the Bragg waves, a larger modulation of backscattered radar power, and a greater image contrast or the modulation depth. Furthermore, since the relaxation rate decreases with wind speed, the image contrast should be

Underwater Topography

higher for low wind speeds than for high wind speeds. Indeed, this prediction of the first-order theory has been confirmed by many observations

However, the first order theory has shortcomings; the most severe one is that it cannot explain the large image contrast (modulation depth) observed in ERS SAR images of underwater bottom topography. On ERS SAR images, the image contrast should be at least a factor of four smaller than on the SEASAT SAR images.

Therefore, a more refined model must be developed. The model needs to take into account that not only the Bragg waves are modulated by the variable surface current associated with the underwater bottom topography, but that the whole wave spectrum is affected. Although the Bragg waves are responsible for the radar backscattering, they are tilted and hydrodynamically modulated by the other waves, in particular by the intermediate-scale waves, i.e., by those waves which have wavelengths typically an order of magnitude larger than the Bragg waves [*Lyzenga and Bennett, 1988, Romeiser et al., 1997, Romeiser and Alpers, 1997*]. Since the tilt modulation is polarization dependent, this refined radar backscattering model, called composite surface model, predicts that the modulation depth at horizontal polarization is larger than at vertical polarization [for details see *Romeiser and Alpers, 1997*].

A further improvement of this composite surface model over the first-order model of *Alpers and Hennings [1984]* and *Shuchman et al., [1985]* is that it yields comparable modulation depths at L- and X-band, which is in agreement with observations. However, it still underestimates somewhat the measured modulations at high radar frequencies, in particular the strong positive modulations in convergent current regions. Better agreement with observations is probably obtained when in the action balance equation the source term is augmented by a term describing the wind modulation and wave breaking [*R. Romeiser, private communication, 2003*].

10.5 Generation of bathymetric maps using SAR images

As stated already in the introduction, there exists quite a demand worldwide for bathymetric surveying. The commercial users include construction companies, oil companies, pipeline and cable companies, and the government users include harbor and shipping control authorities, resource-mapping agencies, and coastal protection agencies. The market is of a considerable size: the total value of bathymetry services in 1995 was estimated to be between 0.8 and 1 billion US dollars. Conventionally, bathymetric surveying is carried out by dedicated ships sailing along tracks with a lateral spacing dependent on the level of precision required for the customer. Sometimes depth accuracy of 30 cm is required.

Since depth measurements carried out from ships are quite expensive, it is a challenge to find a way to reduce the number of sailed tracks without reducing the accuracy of the depth measurements. Here SAR imagery comes into play, which can be used to interpolate depth values between tracks sailed by the survey vessel. In some cases track spacing can be increased by up to a factor of 10, which leads to significant cost savings.

A further factor to be considered is that the SAR data can be used to accurately interpolate measurements into regions such as estuaries where survey ships could experience difficulties. The surveys can therefore be completed at a reduced level of risk to the crew. Finally, in terms of update times, spaceborne SAR imagery is frequently available because the satellite which carries the SAR revisits a specific area typically every few weeks allowing for regular updates of bathymetry maps for areas where the bathymetry can experience rapid change (e. g., shipping channels subject to sediment deposition).

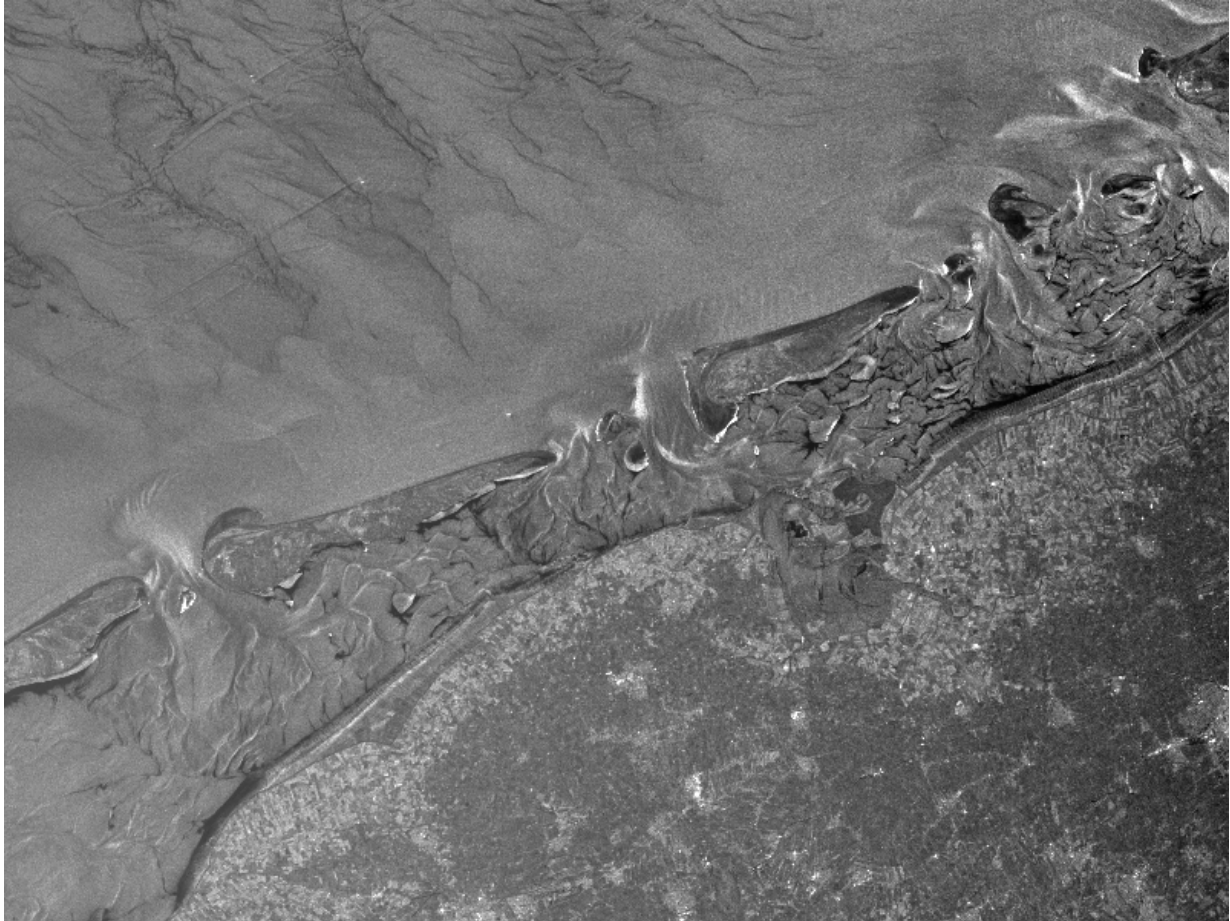


Figure 10.10. ERS-1 (C-band, VV) SAR image of the Waddenzeelands acquired on 3 August 1995. The imaged area is 100 km x 100 km. Between the land (lower section of the image) and the open sea (upper section) several islands are located. The Plaatgat area is located approximately in the center of the image. ©ESA 1995

A method to incorporate SAR images in conventional bathymetric surveying has been developed by ARGOSS in the Netherlands called the Bathymetry Assessment System (BAS). For inverting SAR images into bathymetric maps, additional data are needed for calibration. [Vogelzang *et al.*, 1997; Wensink and Campbell, 1997]

In their inversion scheme, the depth profiles are retrieved from the SAR data in an iterative process such that the closest possible correspondence between modeled and measured depth profiles is obtained. This is achieved by defining a cost (or penalty) function calculated from the weighted sum of the squares of the differences between model predictions and measurements at all grid points within the area to be mapped. The following data are assimilated into BAS: (1) sonar sounding data along calibration tracks to allow tuning, (2) tidal data relating to the acquisition time of the SAR image, (3) wind speed and direction relating to the acquisition time of the SAR image, and (4) the SAR image.

In several validation experiments, it has been shown that this inversion scheme yields fine-grid bathymetric maps with depth accuracy better than 30 cm in accordance with user requirements.

In the following, we present an example of bathymetric surveying carried out in Dutch coastal waters by using sounding data from a ship and an ERS SAR image. The test area is

Underwater Topography

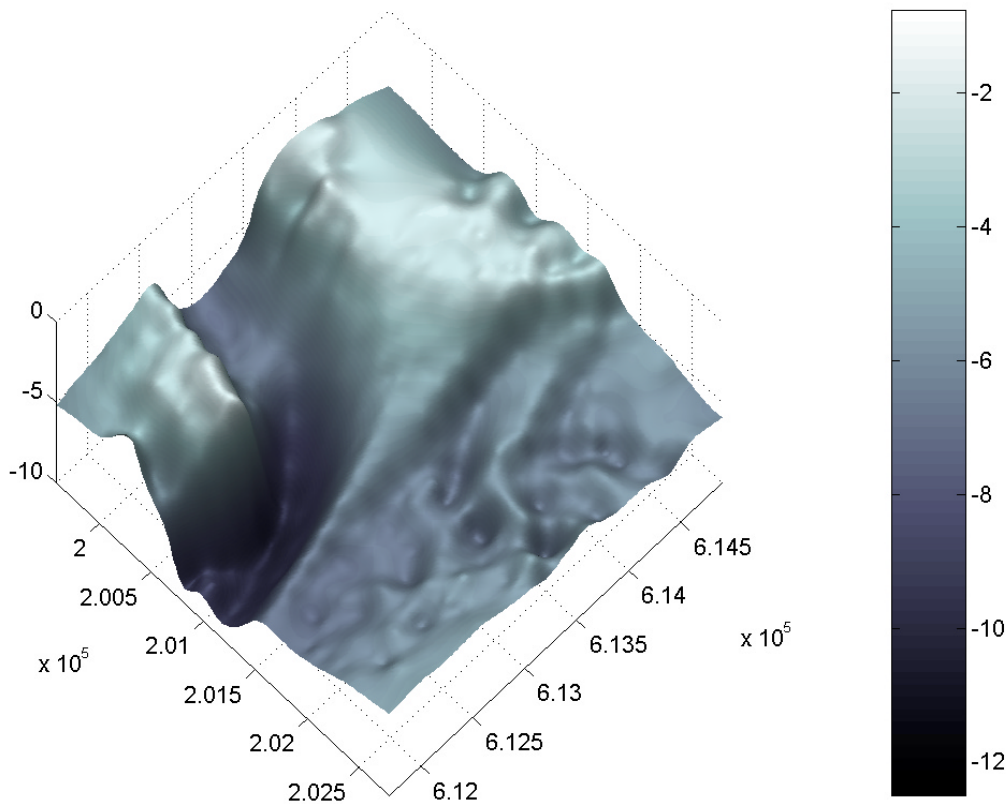


Figure 10.11. Reference seabed elevation surface ("base chart") interpolated from all soundings (tracks are 200 m apart).

located in the Plaatgat area, which is a tidal inlet between the islands of Ameland and Schiermonnikoog in the Waddenzee north of the Netherlands. It has been used extensively to test the skill of tidal flow models, radar imaging models, and bathymetry assessment models because the seabed topography in this area is very complex and has many features such as tidal flats, deep, curved channels, sand waves, and an ebb delta. Another advantage is that detailed depth measurements and many SAR images of this area are available.

Figure 10.10 shows an ERS-1 SAR acquired over this area on 3 August 1995 at 1035 UTC. The dimension of the imaged area is 100 km x 100 km. At that time, the wind was about 5 m s^{-1} from the north. Depth-averaged currents at two points from a tidal simulation were used to guide the high-resolution current simulation within the depth retrieval procedure.

An area of 2 km x 3.2 km in the central part of the Plaatgat area has been chosen for a detailed comparison. In order to assess the amount of information retrieved from the SAR image, two depth charts were compared: (1) a depth chart retrieved from the SAR image and the reduced set of sounding data, and (2) a chart obtained by interpolation of the reduced set of soundings. In addition, a "base chart" interpolated from the full set of soundings (along tracks at a distance of 200 m) was prepared for comparison (see Figure 10.11).

In Figure 10.12, the seabed surfaces obtained with and without SAR image are shown. These figures give a qualitative impression of the information that the SAR image adds to the interpolation of calibration soundings. The elevation surface interpolated from the calibration

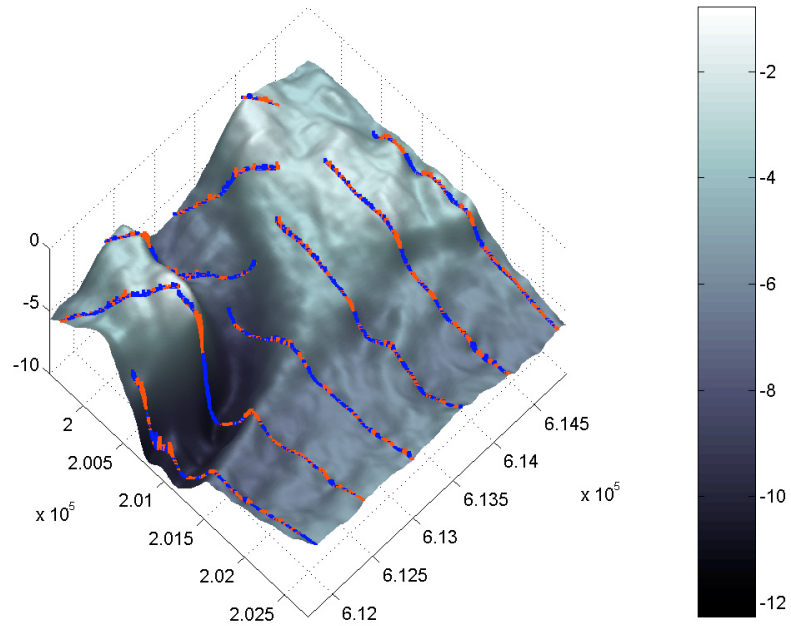


Figure 10.12a. Seabed elevation surface retrieved from SAR image and calibration soundings (tracks are 600 m apart). Deviations between the calibration soundings and the surface are shown as colored bars (red: sample above surface; blue: sample below surface).

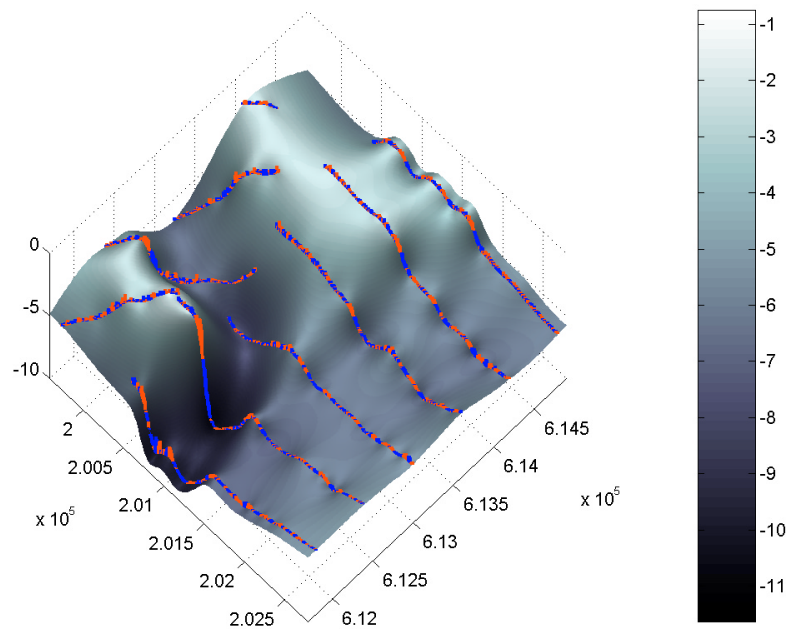


Figure 10.12b. Seabed elevation surface interpolated from calibration soundings (tracks are 600 m apart). Deviations between the calibration soundings and the surface are shown as colored bars (red: sample above surface; blue: sample below surface).

Underwater Topography

(Figure 10.12b) shows the main features of the Plaatgat area: the shoal in the south-west (left in image), the ebb delta in the north and the main channel curving through the shallow parts. However, these features are rounded and blurred. The surface based on the SAR image (Figure 10.12a) shows fine-scale features and, for instance, the shape of the channel agrees much better with the base chart (Figure 10.11). Figures 10.12a and 10.12b also show the deviations from the calibration soundings.

The root-mean-square (rms) difference between the depth surface retrieved from the SAR image and the validation sounding data (along tracks at 200-m distance) is 0.36 m. Without the SAR image, a rms of 0.47 was obtained. This means that the addition of the SAR image has reduced the mean square error by over 40%.

10.6 Summary

It has been known for more than thirty years that, under certain conditions, synthetic aperture radar has the ability to detect sea floor topographic features in shallow water areas. The radar detects underwater features indirectly by means of variations of the sea surface roughness induced by variations of a current overflowing the submarine feature. Thus this technique relies on the presence of a (strong) current, along with small-scale waves (wind waves) on the sea surface to provide the radar backscatter. While at present it is not possible to generate depth charts from radar data alone (acoustic sounding data have to be used for calibration), the data can be used to highlight areas of significant change, or to interpolate between depth profiles measured by acoustic sounders operated from ships.

Finally a remark on how important good knowledge about underwater bottom topography can be. The fact that this paper is written in English and not in Spanish can be linked to it. If, in 1588, the Spanish Fleet, the Armada, had not been defeated by the English Fleet in the English Channel then, very likely, the official language in the U.S. today would be Spanish, and not English. The records of this battle reveal that the Spanish fleet had great difficulty maneuvering in the waters at the southern coast of the English Channel, where many shallow sandbanks are located. One of the leading ships of the Armada, the San Lorenzo, stranded on a sand bank near the harbor of Calais (France) on 8 August 1588 and was immediately set on fire by English sailors assaulting the ship [Padfield, 1988]. According to historians, this event was the turning point of this famous sea battle from which England emerged as the leading colonial World power that paved the way for the Britons to colonize North America and spread the English language to the New Continent.

10.7 References

- Alpers, W., and I. Hennings, 1984: A theory of the imaging mechanism of underwater bottom topography by real and synthetic aperture radar. *J. Geophys. Res.*, **89**, 10 529–10 546.
- de Loor, G. P., 1981: The observation of tidal patterns, currents, and bathymetry with SLAR imagery of the sea. *IEEE J. Oceanic Eng.*, **6**, 124–129.
- , and H.W. Brunsveld van Hulten, 1978: Microwave Measurement in the North Sea. *Bound.-Layer Meteor.*, **13**, 119-131
- Donelan, M. A., and W. C. Pierson, 1987: Radar scattering and equilibrium ranges in wind generated waves with application to scatterometry. *J. Geophys. Res.*, **92**, 4971–5029.
- Hennings, I., R. Doerffer, and W. Alpers, 1988: Comparison of submarine relief features on a radar satellite image and on a Skylab satellite photograph. *Int. J. Remote Sens.*, **9**, 45–67.

- Loder, J. W., 1980: Topographic rectification of tidal currents on the sides of Georges Bank. *J. Phys. Oceanogr.*, **10**, 1399–1416.
- , D. Brickman, and E. P. W. Horne, 1992: Detailed structure of currents and hydrography on the northern side of Georges Bank. *J. Geophys. Res.*, **97**, 14 331–14 351.
- Lodge, D. W. S., 1983: Surface expressions of bathymetry on Seasat synthetic aperture radar images. *Int. J. Remote Sens.*, **4**, 639–653.
- Longuet-Higgins, M. S, and R. W. Stewart, 1964: Radiation stresses in water waves, a physical discussion with applications. *Deep Sea Res.*, **11**, 529–562.
- Lyzenga, D. R., and J. R. Bennett, 1988: Full-spectrum modeling of synthetic aperture radar internal wave signatures. *J. Geophys. Res.*, **93**, 12 345–12 354.
- Padfield, P., 1980: *Armada: A Celebration of the Four Hundreth Anniversary of the Defeat of the Spanish Armada, 1588–1988*. Victor Gollancz Ltd., 208 pp.
- Romeiser, R., and W. Alpers, 1997: An improved composite surface model for the radar backscattering cross section of the ocean surface, 2, Model response to surface roughness variations and the radar imaging of underwater bottom topography. *J. Geophys. Res.*, **102**, 25 251–25 267.
- Shuchman, R. A., D. R. Lyzenga, and G. A. Meadows, 1985: Synthetic aperture radar imaging of ocean-bottom topography via tidal-current interactions: Theory and observations. *Int. J. Remote Sens.*, **6**, 1179–1200.
- Thompson, D. R, and R. F. Gasparovic, 1986: Intensity modulation in SAR images of internal waves. *Nature*, **320**, 345–348.
- Trulsen, G. N., K. B. Dysthe, and J. Trulsen, 1990: Evolution of a gravity wave spectrum through a current gradient. *J. Geophys. Res.*, **95**, 22 141–22 151.
- Valenzuela, G. R., 1978: Theories for the interaction of electromagnetic and ocean waves—A review. *Bound.-Layer Meteor.*, **13**, 61–85.
- , W. J. Plant, D. T. Chen, W. C Keller, and D. L Schuler, 1985: Microwave probing of shallow water bottom topography in the Nantucket Shoals. *J. Geophys. Res.*, **90**, 4931–4942.
- Vogelzang, J., 1997: Mapping submarine sand waves with multi-band imaging radar, 1. Model development and sensitivity analysis. *J. Geophys. Res.*, **102**, 1163–1181.
- , G. J. Wensink, G. P. de Loor, H. C. Peters, and H. Pouwels, 1992: Sea bottom topography with X band SLAR: the relation between radar imagery and bathymetry. *Int. J. Remote Sens.*, **13**, 1943–1958.
- , G. J. Wensink, C. J. Calkoen, and M. W. A. van der Kooij, 1997: Mapping submarine sand waves with multi-band imaging radar, 2, Experimental results and model comparison. *J. Geophys. Res.*, **102**, 1183–1192.
- Weissman, D. E., W. J. Plant, and S. Stolte, 1996: The response of microwave cross sections of the sea to wind fluctuations. *J. Geophys. Res.*, **101**, 12 149–12 161.
- Wensink, H., and G. Campbell, 1997: Bathymetric map production using the ERS SAR. *Backscatter*, **8**, 17–22.